PHYSICAL REVIEW FLUIDS **8**, 054608 (2023)

Multiscale flow topologies in microconfined high-pressure transcritical fluid turbulence

Guillem Barea, Núria Masclans, and Lluís Jofre[*]
Department of Fluid Mechanics, Universitat Politècnica de Catalunya · BarcelonaTech (UPC), Barcelona 08034, Spain

(Received 31 March 2023; accepted 1 May 2023; published 30 May 2023)

The topology of multiscale turbulent motions in a high-pressure transcritical channel flow is studied using direct numerical simulations. In particular, the system analyzed corresponds to high-pressure ($P/P_c = 2$) microconfined turbulence of N_2 at transcritical conditions imposed by a temperature difference between the cold ($T/T_c = 0.75$) and hot ($T/T_c = 1.5$) walls for a friction Reynolds number of $\mathrm{Re}_\tau = 100$ (cold wall). The invariants of the velocity-gradient, rate-of-strain, and rate-of-rotation tensors are computed at different length scales. The joint probability density functions of the invariants are calculated and conditioned based on the distance from the walls and additionally compared against an equivalent low-pressure case at isothermal conditions. The results indicate that the presence of higher levels of vorticity close to the hot wall significantly impacts the flow topologies in the viscous sublayer. As a result, topology distributions of the velocity-gradient tensor typical from the outer region are observed in the vicinity of the hot wall. Moreover, the second invariants of the rate-of-strain and rate-of-rotation tensors indicate a large probability of vortex sheet events in the hot (supercritical gaslike) region. Finally, at lengths comparable to the density gradient scale, the presence of vortex sheet structures is diminished with respect to the reference low-pressure case to favor more tubelike flow motions. As inferred from the vorticity transport equation, this behavior is connected to the appearance of a baroclinic-type instability generated from the combination of the external force driving the flow and the large variation of density across the pseudoboiling region.

DOI: 10.1103/PhysRevFluids.8.054608

I. INTRODUCTION

From innovative biomedical solutions to powerful sophisticated microchips, technology has become microscopically compact over the past decades. This trend has been particularly important in the field of microfluidics which has extraordinarily branched into a virtually infinite number of applications due to its high surface-to-volume ratios, flow controllability, and length scales efficiently suited for interacting with microscopic elements. These properties have proven to be well-suited, for example, to biology and chemistry, in which localized precision is usually an advantage. However, the utilization of microfluidics for energy applications has long been a key challenge in what some researchers refer to as "*lab-on-a-chip and energy—the microfluidic frontier*" [1]. One of the principal reasons is that standard microfluidic systems are typically limited to operate under laminar

---

[*] lluis.jofre@upc.edu

flow regimes due to their small characteristic hydraulic diameters [$D_h \sim 1$–1000 μm] and bulk velocities [$u_b \sim \mathcal{O}(1)$ m/s]. In particular, at atmospheric pressure conditions, the Reynolds numbers encountered in microfluidics are in the order of $\mathrm{Re}_b = u_b D_h/\nu \sim 0.1$–$100$, where $\nu \sim 10^{-6}$–10^{-4} m^2/s are typical values for the kinematic viscosity, and consequently flows tend to remain laminar [2]. The smooth nature of this flow regime does not provide good mixing and transfer efficiencies in comparison to the performances obtained if turbulence, which is characterized by rapid fluctuations of flow variables in space and time, is present [3]. In this regard, an important body of research in microfluidics is focused on improving molecular diffusion in laminar flows through different passive-mixing strategies [4–6], like, for example, fabricating serpentinelike microchannels and cross-/patterned-flow mixers. However, these techniques typically impose important construction complexities without exceptional increases in mixing and transfer rates. Other strategies significantly explored try to (i) achieve enhanced chaotic mixing through electrokinetic forcing [7] or (ii) reach incipient turbulent flow conditions by extraordinarily increasing the volumetric flow rates (large sizes/velocities) [8], which is in contradiction to the small values typically sought in microfluidic applications. Moreover, connected to this topic, experimental studies are commonly conducted using micro-particle image velocimetry (microPIV). This methodology enables the observation and characterization of flows at the microscale, like, for example, near-wall mechanisms [9–11], two-phase flow phenomena [12–14], and laminar-to-turbulent transition [15,16].

A novel potential approach to achieve microconfined turbulence, which is carefully studied by Bernades *et al.* [17,18], is based on operating under high-pressure supercritical conditions to leverage the hybrid thermophysical properties of supercritical fluids. High-pressure supercritical fluids are used in a wide range of engineering applications, like, for example, in gas turbines, supercritical water-cooled reactors, and liquid rocket engines [19,20]. They operate within high-pressure thermodynamic spaces in which intermolecular forces and finite packing volume effects become important. In this regard, it is important to distinguish between supercritical gaslike and liquidlike fluids separated by the pseudoboiling line [21]: (i) a supercritical liquidlike fluid is one whose density is large, and whose transport coefficients behave similarly to a liquid; whereas (ii) the density of supercritical gaslike fluids is smaller, and their transport coefficients vary similar to gases. In particular, the strategy proposed makes use of the rapid smooth transition when crossing the pseudoboiling line to tune supercritical fluids to present liquidlike densities [$\rho \sim 10^3$ $\mathrm{kg/m}^3$] and gaslike viscosities [$\mu \sim 10^{-5}$ Pa s], and therefore achieve $\mathrm{Re}_b \sim 10^3$–10^4 for typical microfluidic velocities and channel sizes and favoring, in this manner, inertial over viscous forces and resulting in turbulent flow [2]. The theoretical estimations presented in their work indicate that microconfined turbulent flow regimes can be potentially achieved by operating in the vicinity of the pseudoboiling region for a wide range of popular working fluids, like, for example, carbon dioxide, methane, nitrogen, oxygen, and water. In this regard, the experimental study of supercritical fluids is notably challenging due to the high pressures typically involved, which significantly limit the quantity and quality of data that can be extracted from laboratory experiments and/or industrial applications [22]. This complexity is further increased by the interest in working in microfluidics conditions. Consequently, this work will utilize computational approaches based on direct numerical simulation (DNS) to resolve all turbulent scales and further analyze them. In connection with this strategy, Zhang *et al.* [23] explored mixing intensification for antisolvent processes by operating at high pressures in free-shear coflow configurations at isothermal conditions. Nonetheless, the overall strategy is significantly different to the one studied in this work as: (i) jet flows are inherently unstable, and consequently laminar-to-turbulent transition occurs in the range $\mathrm{Re}_b \approx 30$–2000 [24]; (ii) coflows require complex microfluidic configurations; and (iii) isothermal conditions are not generally suitable for energy-related applications.

The detailed flow characterization and modeling of high-pressure transcritical fluid turbulence remain an outstanding challenge [19] due to the presence, especially, of localized large density gradients that may modulate the flow [21]. Moreover, these density gradients tend to modify the near-wall characteristics of turbulent flow as shown by different authors [25–28]. In this regard, novel approaches have been proposed to carefully study transformations of flow statistics for the mean velocity profile [29–31] and mean temperature distribution [28,32,33]. Consequently, the development of predictive, coarse-grained models for the design and optimization of engineering applications, like, for example, Reynolds-averaged Navier-Stokes (RANS) approaches, remains an open problem. It is now well established that, since the large-scale features of turbulence are typically flow dependent, different models are needed for different flows [34]. However, a major motivation for the development of large-eddy simulation (LES) approaches is the belief that, although large structures may vary between flows, at smaller scales the features should be less flow-dependent and more amenable to modeling. Universal fine-scale features, if they can be identified, should potentially be of greater utility in construction of subgrid-scale (SGS) models [35,36] than broad assumptions concerning statistical isotropy of turbulent fluctuations at high wave numbers. For instance, in the case of high-pressure transcritical turbulence, it is unclear whether the small and/or intermediate scales are universal and statistically isotropic. Nevertheless, using local topology, or streamline patterns, is a highly effective method for characterizing flow features and regimes, efficiently quantifying the deformation and mixing of fluid elements and making it notably useful in this regard. For example, a strain-dominated streamline pattern will deform a fluid element and lead to increased mixing, while a rotation-dominated pattern, however, will merely reorient a fluid element without much increase in mixing. Motivated by the need for a general methodology, Perry *et al.* [37,38] proposed a scheme based on the three invariants (P, Q, R) of second-order tensors to effectively infer local flow topologies in velocity fields. Subsequently, Soria *et al.* [39], using DNS results, studied the joint statistical distributions of Q and R in mixing layers. They found that the scatter plot of second and third invariants (i) presents small amounts of data in the lower right quadrant, whereas (ii) the bulk of data lies in the upper left and lower right quadrants roughly distributed uniformly over an elliptical region. The local topologies associated with these two regions are unstable node/saddle/saddle and stable focus stretching (described in detail later). These prominent topological features immediately attracted considerable research attention and were later found to be quite general across a variety of turbulent flows. Examples of such studies include high-symmetry flows [40], turbulent channel flows [41], turbulent jets [42], two-phase turbulence [43], and compressible flows [44]. For a review of the dynamics of small-scale turbulence and various modeling approaches the reader is referred to the article by Meneveau [45].

The aim of this work, therefore, is to thoroughly study and characterize the multiscale flow topologies of high-pressure transcritical fluid turbulence by means of carefully analyzing the invariants of the velocity-gradient tensor using joint probability density functions (JPDFs). In particular, focus will be placed on the case of wall-bounded turbulent flows at low (subcritical) and high (supercritical) pressure conditions; for the high-pressure system, a temperature difference is imposed between walls, whereas the system is isothermal for the low-pressure case. To that end, the paper is organized as follows. In Sec. II, the classification of local flow topologies based on velocity-gradient tensor invariants is presented. This is followed by a detailed description of the flow physics modeling utilized to study high-pressure transcritical fluid turbulence in terms of equations of fluid motion, real-gas thermodynamics, and numerical methods in Sec. III. Next, in Sec. IV, computational experiments are described and results regarding the flow topology at different scales are discussed. The aim is to characterize how transcritical conditions affect the turbulent flow topologies using JPDFs. In addition, the different terms of the vorticity transport equation are studied to further connect the flow typologies observed with the underlying flow mechanisms. Finally, the work is concluded and future directions are proposed in Sec. V.

II. CLASSIFICATION OF LOCAL FLOW TOPOLOGY

The theoretical work that connected invariants of the velocity-gradient tensor to flow topologies was established by Perry *et al.* [37,38]. They employed critical point theory (i.e., local streamlines have an indeterminate slope) to relate the invariants of the velocity-gradient tensor to the local three-dimensional flow field as seen by an observer traveling with the flow. In this regard, the

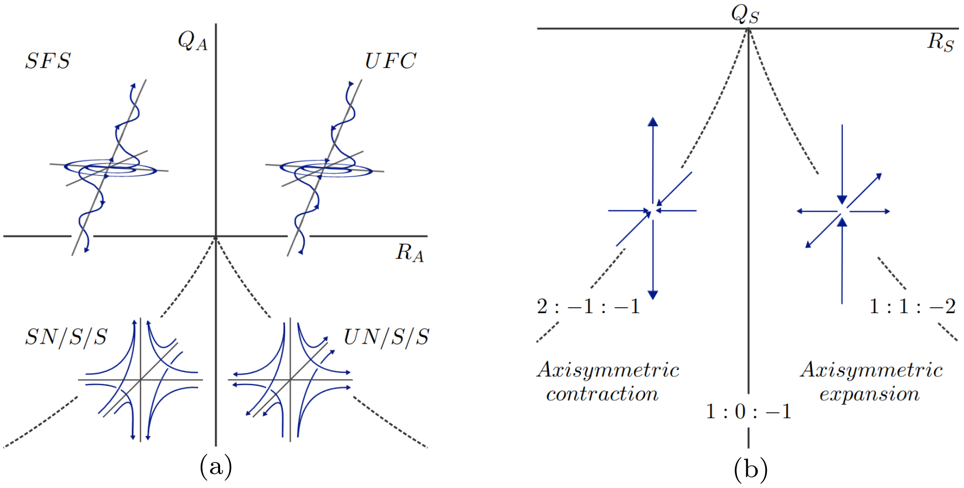

FIG. 1. Topological classification of local flow fields (streamlines) for an observer traveling with the flow on the R_A versus Q_A diagram (a): upper-left, stable focus/stretching (SFS); upper right, unstable focus/compressing (UFC); lower left, stable node/saddle/saddle (SN/S/S); lower right, unstable node/saddle/saddle (UN/S/S). Lines in (R_S, Q_S)-space corresponding to different ratios of principal strains $\lambda_1 : \lambda_2 : \lambda_3$ (b): $2 : -1 : -1$, axisymmetric contraction; $1 : 0 : -1$, two-dimensional straining limit; $1 : 1 : -2$, axisymmetric expansion.

subsections below summarize the theoretical framework of the tensor-invariant-based flow topology classification for completeness of the present work and to introduce the notation utilized.

A. Invariants of the velocity-gradient tensor

The velocity-gradient tensor $A_{ij} = \partial u_i/\partial x_j$ can be decomposed into rate-of-strain S_{ij} (symmetric) and rate-of-rotation W_{ij} (skew-symmetric) tensors written in the form

$$S_{ij} = \frac{1}{2}\left(\frac{\partial u_i}{\partial x_j} + \frac{\partial u_j}{\partial x_i}\right) \quad \text{and} \quad W_{ij} = \frac{1}{2}\left(\frac{\partial u_i}{\partial x_j} - \frac{\partial u_j}{\partial x_i}\right), \tag{1}$$

such that $A_{ij} = S_{ij} + W_{ij}$. The coefficients $(P_A,\ Q_A,\ R_A)$ multiplying the eigenvalues λ_i of the characteristic equation of A_{ij}, written in the form

$$\lambda_i^3 + P_A\lambda_i^2 + Q_A\lambda_i + R_A = 0, \tag{2}$$

are the tensor invariants, which correspond to

$$P_A = -\mathrm{tr}[A_{ij}] = -S_{ii}, \tag{3}$$

$$Q_A = \tfrac{1}{2}\big(P_A^2 - \mathrm{tr}\big[A_{ij}^2\big]\big) = \tfrac{1}{2}\big(P_A^2 - S_{ij}S_{ji} - W_{ij}W_{ji}\big), \tag{4}$$

$$R_A = \tfrac{1}{3}\big(-P_A^3 + 3P_AQ_A - \mathrm{tr}\big[A_{ij}^3\big]\big) = \tfrac{1}{3}\big(-P_A^3 + 3P_AQ_A - S_{ij}S_{jk}S_{ki} - 3W_{ij}W_{jk}S_{ki}\big). \tag{5}$$

The topological features of the velocity-gradient tensor as a function of position in (P_A, Q_A, R_A) space can be classified according to the value of the discriminant

$$D_A = 27{R_A}^2\big(4P_A^3 + 18P_AQ_A\big)R_A + \big(4{Q_A}^3 - P_A^2Q_A^2\big), \tag{6}$$

which determines the real/imaginary nature of the eigenvalues of A_{ij}. As illustrated in Fig. 1(a), for low-Mach-number flows in which $|P_A| \ll 1$, a positive discriminant $D_A > 0$ corresponds to one real and two complex-conjugate eigenvalues (enstrophy prevalence); a negative discriminant $D_A < 0$

gives rise to three real, distinct eigenvalues (dissipation prevalence); and a zero-valued discriminant $D_A = 0$ indicates three real eigenvalues of which two are equal. A further classification can be made according to the sign of R_A. On the left half of the (Q_A, R_A) plane the real parts of the complex-conjugate eigenvalues are negative and the critical points of the flow are classified as stable, while on the right half-plane, the real part of the eigenvalues are positive and the critical points are classified as unstable. The physical interpretation of R_A depends on the sign of D_A. On the one hand, if $D_A > 0$, then $R_A < 0$ implies a predominance of vortex stretching over vortex compression (the opposite is true for $R_A > 0$). On the other hand, if $D_A < 0$, then $R_A > 0$ is associated with converging flow trajectories, whereas $R_A < 0$ is connected to diverging flow trajectories. Following Chong *et al.* [38] terminology, critical point topologies falling in the upper left (right) region are called stable (unstable) focus/stretching (compressing), and those in the lower left (right) region are referred to as stable (unstable) node/saddle/saddle.

B. Invariants of the rate-of-strain and rate-of-rotation tensors

The local topology of any second-order tensor field, such as S_{ij} and W_{ij}, can be classified as described above. Owing to the symmetry of S_{ij}, all eigenvalues are real. Hence, in the case of low-Mach-number flows, only classifications for which $D_S \leqslant 0$ can be obtained on the (R_S, Q_S)-plane as shown in Fig. 1(b). In particular, all (R_S, Q_S) pairs must fall below the lines corresponding to the eigenvalue ratios (eigenvalues of S_{ij} λ_1, λ_2, λ_3 in descending order) $2 : -1 : -1$ (axisymmetric contraction) and $1 : 1 : -2$ (axisymmetric expansion). The ratio $1 : 0 : -1$ corresponds to the two-dimensional straining limit. Note also that the local dissipation rate of turbulent kinetic energy (TKE) ε and enstrophy ω can be expressed in terms of Q_S and Q_W as $\varepsilon = 2\nu S_{ij}S_{ij} = -4\nu Q_S$ and $\omega = 2W_{ij}W_{ij} = 4Q_W$, respectively, with ν the kinematic viscosity of the fluid. Therefore, regions corresponding to large negative values of Q_S are sites of high dissipation, while large values of Q_W indicate flow regions characterized by high vorticity.

In addition, the second invariant of A_{ij}, $Q_A = Q_S + Q_W$, is a measure of the relative importance of the straining and rotational parts of the velocity-gradient tensor. In regions of the flow in which Q_A is large and positive, vorticity is high and dominates the strain rate, while the reverse is true if Q_A is large and negative. This relative importance can be directly visualized by plotting Q_W against $-Q_S$. Points which lie near the Q_W axis are in the nearly pure solid-body rotation, whereas points that lie near the $-Q_S$ axis have nearly pure straining motions. Points around the 45° line, where strain rate and rotation are of the same order, correspond to regions of the flow dominated by sheetlike motions, like those found in boundary layers and represented in Fig. 2(a); viz. sheetlike topologies present similar rates of strain and rotation, and therefore are dissipative-dominated flow structures [39]. On the contrary, vortex tubelike structures, as illustrated in Fig. 2(b), are characterized by low dissipation rates due to the decrement of straining with respect to rotation.

III. FLOW PHYSICS MODELING

The framework utilized for studying microconfined supercritical fluids turbulence in terms of (i) equations of fluid motion, (ii) real-gas thermodynamics, (iii) high-pressure transport coefficients, and (iv) numerical method are described below.

A. Equations of fluid motion

The turbulent flow motion of supercritical fluids is described by the following set of conservation equations of mass, momentum, and total energy

$$\frac{\partial \rho}{\partial t} + \nabla \cdot (\rho \boldsymbol{u}) = 0, \tag{7}$$

$$\frac{\partial (\rho \boldsymbol{u})}{\partial t} + \nabla \cdot (\rho \boldsymbol{u}\boldsymbol{u}) = -\nabla P + \nabla \cdot \boldsymbol{\tau} + \boldsymbol{f}, \tag{8}$$

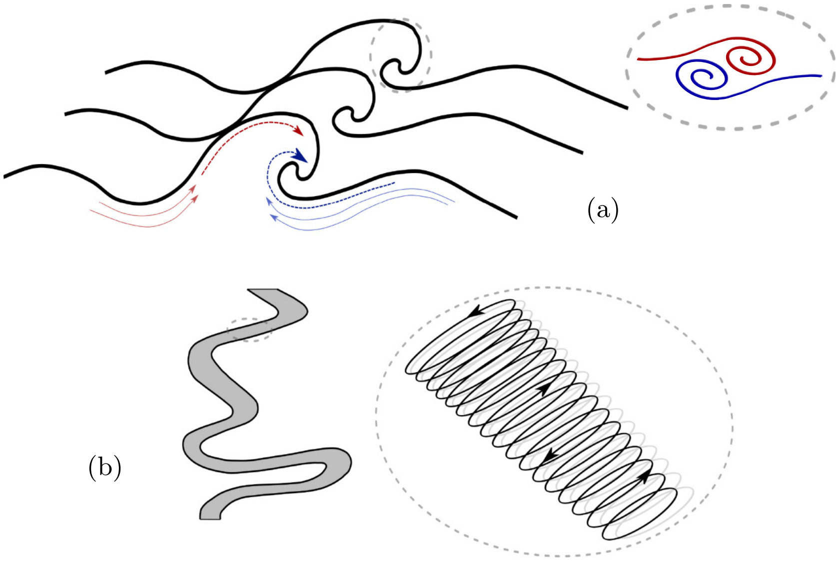

FIG. 2. Schematic representation of (a) vortex sheet and (b) vortex tube structures.

$$\frac{\partial(\rho E)}{\partial t} + \nabla \cdot (\rho \boldsymbol{u} E) = -\nabla \cdot \boldsymbol{q} - \nabla \cdot (P\boldsymbol{u}) + \nabla \cdot (\boldsymbol{\tau} \cdot \boldsymbol{u}) + \boldsymbol{f} \cdot \boldsymbol{u}, \tag{9}$$

where ρ is the density, $\boldsymbol{u}$ is the velocity vector, P is the pressure, $\boldsymbol{\tau} = \mu(\nabla\boldsymbol{u} + \nabla\boldsymbol{u}^T) - (2\mu/3)(\nabla \cdot \boldsymbol{u})\boldsymbol{I}$ is the viscous stress tensor with μ the dynamic viscosity and $\boldsymbol{I}$ the identity matrix, $\boldsymbol{f}$ is a general force (source term), E is the total energy, and $\boldsymbol{q} = -\kappa\nabla T$ is the Fourier heat conduction flux with κ the thermal conductivity.

B. Real-gas thermodynamics

The thermodynamic space of solutions for the state variables pressure P, temperature T, and density ρ of a monocomponent fluid is described by an equation of state. One popular choice for systems at high pressures, which is used in this study, is the Peng-Robinson [46] equation of state written as

$$P = \frac{R_u T}{\bar{v} - b} - \frac{a}{\bar{v}^2 + 2b\bar{v} - b^2}, \tag{10}$$

with R_u the universal gas constant, $\bar{v} = W/\rho$ the molar volume, and W the molecular weight. The coefficients a and b take into account real-gas effects related to attractive forces and finite packing volume, respectively, and depend on the critical temperatures T_c, critical pressures P_c, and acentric factors ω. They are defined as

$$a = 0.457\frac{(\mathrm{R_u} T_c)^2}{P_c}[1 + c(1 - \sqrt{T/T_c})]^2, \tag{11}$$

$$b = 0.078\frac{\mathrm{R_u} T_c}{P_c}, \tag{12}$$

where coefficient c is provided by

$$c = \begin{cases} 0.380 + 1.485\omega - 0.164\omega^2 + 0.017\omega^3 & \text{if } \omega > 0.49, \\ 0.375 + 1.542\omega - 0.270\omega^2 & \text{otherwise.} \end{cases} \tag{13}$$

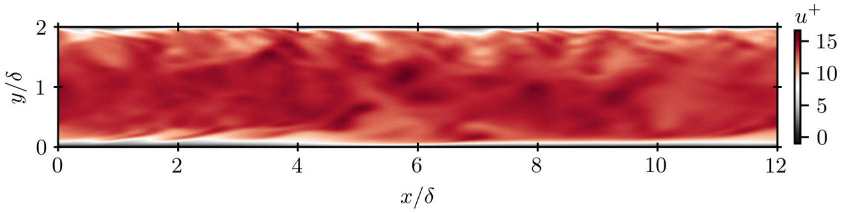

FIG. 3. Snapshot of instantaneous streamwise velocity in wall units u^+ on a x-y slice.

The Peng-Robinson real-gas equation of state needs to be supplemented with the corresponding high-pressure thermodynamic variables based on departure functions [47] calculated as a difference between two states. In particular, their usefulness is to transform thermodynamic variables from ideal-gas conditions (low pressure—only temperature dependant) to supercritical conditions (high pressure). The ideal-gas parts are calculated by means of the NASA 7-coefficient polynomial [48], while the analytical departure expressions to high pressures are derived from the Peng-Robinson equation of state as detailed, for example, in Jofre and Urzay [20].

C. High-pressure transport coefficients

The high pressures involved in the analyses conducted in this work prevent the use of simple relations for the calculation of the dynamic viscosity μ and thermal conductivity κ. In this regard, standard methods for computing these coefficients for Newtonian fluids are based on the correlation expressions proposed by Chung *et al.* [49,50]. These correlation expressions are mainly function of critical temperature T_c and density ρ_c, molecular weight W, acentric factor ω, association factor κ_a and dipole moment $\mathcal{M}$, and the NASA 7-coefficient polynomial [48]; further details can be found in dedicated works like, for example, Jofre and Urzay [20] and Poling *et al.* [51].

D. Numerical method

The equations of a fluid motion introduced in Sec. III A are numerically solved by adopting a standard semidiscretization procedure; viz. they are first discretized in space and then integrated in time. In particular, spatial operators are treated using second-order central-differencing schemes, and time-advancement is performed by means of a third-order strong-stability preserving (SSP) Runge-Kutta explicit approach [52]. The convective terms are expanded according to the Kennedy-Gruber-Pirozzoli (KGP) splitting [53,54], which has been recently assessed for high-pressure supercritical fluids turbulence [55]. The method preserves kinetic energy by convection and is locally conservative for mass, momentum, and total energy. This numerical framework provides stable computations without the need for any form of artificial dissipation or stabilization procedures.

IV. RESULTS AND DISCUSSION

Microconfined high-pressure transcritical turbulence is studied by means of DNS strategies based on the flow physics framework described in Sec. III. Data is obtained utilizing the in-house compressible flow solver RHEA [56]. The problem setup and discussion of results are described below.

A. Problem setup

As illustrated in Fig. 3, the channel flow setup is chosen to study and characterize high-pressure supercritical fluids turbulence at the microscale. In particular, the fluid selected is N_2, whose critical pressure and temperature are $P_c = 3.4\,\text{MPa}$ and $T_c = 126.2\,\text{K}$. The fluid system is at a supercritical

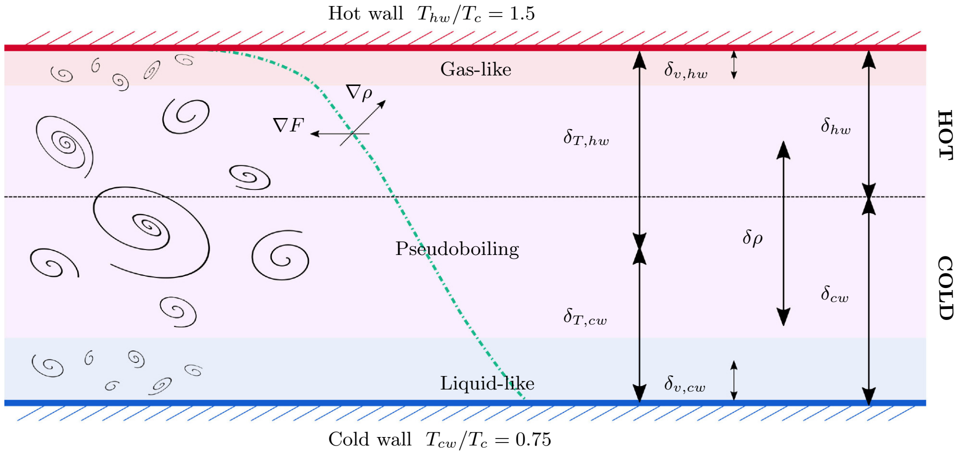

FIG. 4. Hydrodynamic scales of the transcritical turbulent channel flow studied.

bulk pressure of $P_b/P_c = 2$ and confined between cold (cw) and hot (hw) isothermal walls, separated at a distance $H = 2\delta$ with $\delta = 100\ \mu$m the channel half-height, at $T_{\mathrm{cw}}/T_c = 0.75$ and $T_{\mathrm{hw}}/T_c = 1.5$, respectively. This problem setup imposes the fluid to undergo a transcritical trajectory by operating within a thermodynamic region across the pseudoboiling line. Based on preliminary theoretical estimations [2], the friction Reynolds number selected at the cold wall is $\mathrm{Re}_{\tau,\mathrm{cw}} = \rho_{\mathrm{cw}} u_{\tau,\mathrm{cw}} \delta/\mu_{\mathrm{cw}} = 100$, with $u_\tau = \sqrt{(\mu/\rho)(d\langle u\rangle/dy)}$ the friction velocity at walls, to ensure fully developed turbulent flow conditions; the ρ_{cw} and μ_{cw} values are obtained from the thermophysical model described in Sec. III. The mass flow rate in the streamwise direction is imposed through a body force $\boldsymbol{f}$ controlled by a proportional feedback loop (gain $k_p = 0.1$) aimed at reducing the difference between the desired ($\mathrm{Re}_{\tau,\mathrm{cw}} = 100$) and measured (numerical) $\mathrm{Re}_{\tau,\mathrm{cw}}$ values.

The computational domain is $4\pi\delta \times 2\delta \times 4/3\pi\delta$ in the streamwise (x), wall-normal (y), and spanwise (z) directions, respectively. The streamwise and spanwise boundaries are set periodic, and no-slip conditions are imposed on the horizontal boundaries (x-z planes). The grid is uniform in the streamwise and spanwise directions with resolutions in wall units (based on cw values) equal to $\Delta x^+ \approx 9.8$ and $\Delta z^+ \approx 3.3$, and stretched toward the walls in the vertical direction with the first grid point at $y^+ = y u_{\tau,\mathrm{cw}}/\nu_{\mathrm{cw}} \approx 0.1$ and with sizes in the range $0.2 \lesssim \Delta y^+ \lesssim 2.3$. Thus, based on preliminary studies, this grid arrangement corresponds to a DNS of size $128 \times 128 \times 128$ grid points. The simulation strategy starts from a linear velocity profile with random fluctuations [57], which is advanced in time to reach turbulent steady-state conditions after approximately 5 flow-through-time (FTT) units; based on the bulk velocity u_b and the length of the channel $L_x = 4\pi\delta$, an FTT is defined as $t_b = L_x/u_b \sim \delta/u_\tau$. Finally, flow statistics are collected for roughly 10 FTTs once steady-state conditions are achieved.

B. Estimation of hydrodynamic scales

As a first step of the analysis, the hydrodynamic scales of the problem shown in Fig. 4 are estimated based on scaling arguments. In the case of confined turbulent flows, the size of the larger vortical motions are in the order of the channel half-height δ, whereas the smallest flow scales are typically found in the viscous region of the boundary layers and correspond to $\delta_v = \delta/\mathrm{Re}_\tau$. However, in the specific case of this work, due to the temperature difference imposed between the hot and cold walls, the system is not symmetric in the wall-normal direction, and as a result the largest scales correspond to $\delta_{\mathrm{cw}} \approx 107\ \mu\mathrm{m}$ and $\delta_{\mathrm{hw}} \approx 93\ \mu\mathrm{m}$ for the cold and hot regions, respectively. Similarly, the viscous scale at the cold wall is $\delta_{v,\mathrm{cw}} \approx 1\ \mu\mathrm{m}$, while it is virtually halved to $\delta_{v,\mathrm{hw}} \approx 0.5\ \mu\mathrm{m}$ for the hot wall. It is also worth noting the existence of a Batchelor scale related

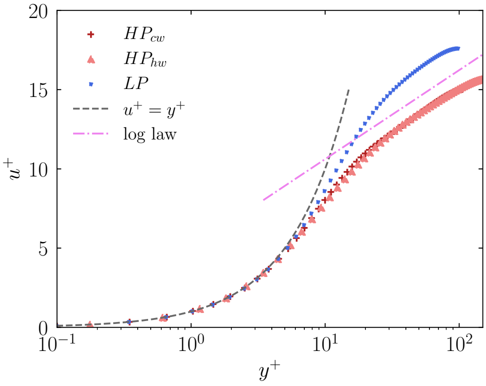

FIG. 5. Time-averaged streamwise velocity u^+ along the wall-normal direction y^+ for the cold (cw) and hot (hw) walls of the high- (HP) and low-pressure (LP) cases.

to temperature variations. This scale can be estimated as $\delta_{T,\text{cw}} \sim \delta_{cw}/\sqrt{Pr_{cw}} \approx 73$ µm for the cold region, while it increases to $\delta_{T,\text{hw}} \sim \delta_{\text{hw}}/\sqrt{Pr_{\text{hw}}} \approx 94$ µm for the hot region.

In the case of high-pressure transcritical systems, an additional length scale $\delta_{\nabla\rho}$ can be defined with respect to the large localized density variations across the pseudoboiling line. In this regard, as proposed by Jofre and Urzay [21], the average density gradient scale is estimated as

$$\delta_{\nabla\rho} \sim \frac{\rho_l - \rho_g}{\langle\|\nabla\rho\|\rangle} \approx 31.4 \ \mu\text{m}, \tag{14}$$

where $\rho_l \approx 574\,\text{kg/m}^3$ and $\rho_g \approx 196\,\text{kg/m}^3$ correspond, respectively, to the supercritical-like liquid and gas density limits of the pseudoboiling region based on the methodology introduced by Wang *et al.* [58], and $\langle\|\nabla\rho\|\rangle$ is the ensemble-averaged value of the density gradients across the domain. Therefore, these results indicate that the density gradient scale is 30× and 60× larger than the viscous scale related to the cold and hot walls, respectively.

C. Characterization of flow statistics

The purpose of this subsection is to characterize the turbulent flow in the high-pressure (HP) transcritical case based on first- and second-order statistics. Particularly, Fig. 5 shows the time-averaged streamwise velocity as a function of distance to the wall in viscous units, whereas Fig. 6 depicts the Favre-averaged fluctuations of the three components of velocity u^+_{rms}, v^+_{rms}, and w^+_{rms}. In addition, the time-averaged profiles for the cold and hot walls are compared against a reference case corresponding to an equivalent isothermal channel setup at low pressure (LP) of $P_b/P_c = 0.03$ with $\text{Re}_\tau = 100$. Based on the results presented in Fig. 5, it can be seen that the three profiles exhibit the typical linear behavior $u^+ = y^+$ of turbulent flows in the viscous sublayer region ($y^+ < 5$). However, the HP profiles deviate to lower values from the LP result starting at the buffer layer ($5 \leqslant y^+ < 35$); to correct these deviations, different transformations have been recently proposed [29–31] that, if adapted to high-pressure transcritical flows, may be applicable. This deviation is gradually accentuated in the log-law region ($y^+ \geqslant 35$), which is indicative that the HP case is characterized by larger turbulent intensities resulting in a more flattened shape of the velocity profile as indicated by the friction Reynolds numbers listed in Table I. However, focusing on the Favre-averaged velocity fluctuations for the high-pressure system depicted in Fig. 6, turbulence intensity is significantly different between the hot (gaslike) and cold (liquidlike) walls in the streamwise direction. In particular, the hot wall presents larger fluctuations in the viscous sublayer and buffer region, while turbulence intensity grows following a concave parabola from the cold wall to the center of the channel. An equivalent, although significantly less pronounced,

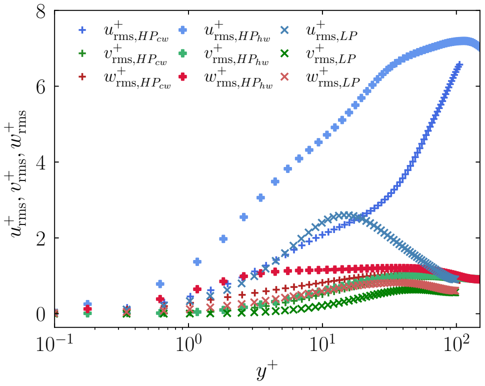

FIG. 6. Favre-averaged fluctuations of velocity u^+_{rms}, v^+_{rms}, and w^+_{rms} along the wall-normal direction y^+ for the cold (cw) and hot (hw) walls of the high- (HP) and low-pressure (LP) cases.

behavior is observed for the fluctuations in the spanwise direction, whereas they virtually collapse to the same curve for the wall-normal velocity. Finally, regarding the LP case, the Favre-averaged velocity fluctuations closely resemble those of Moser *et al.* [59], which report maximum values of streamwise velocity fluctuations in the buffer layer. However, in comparison, the HP system presents significantly larger fluctuations, suggesting a modification of the turbulent characteristics that will be thoroughly investigated in the following sections.

Focusing on the temperature distribution, different behaviors can be observed. In particular, Fig. 7 depicts the time-averaged temperature increment in viscous units $\Delta T^+ = (T - T_w)/T_\tau$, with T_w the wall temperature and $T_\tau = [\kappa/(\rho c_P u_\tau)(d\langle T\rangle/dy)]$, along the wall-normal direction y^+, and Fig. 8 presents the Favre-averaged temperature fluctuations. As indicated by Fig. 7, the time-averaged temperature increment values at the cold wall are roughly 2–4× larger than at the hot wall due to the larger Prandtl number achieved; viz. as listed in Table I, *Pr* is approximately 2× larger at the cold wall. This behavior is mainly a consequence of the higher thermal inertia (larger values of density and specific heat capacity) of the supercritical liquidlike fluid found at the cold part of the channel with respect to the supercritical gaslike fluid occupying the hot region. Additionally, as shown in Fig. 8, the temperature fluctuations are larger at the cold side of the channel in comparison to the hot region. Consequently, the degree of convective-dominated mixing is higher at the cold part, roughly a factor of 4 as indicated by the Nusselt number in Table I, which enhances the transport of supercritical liquidlike fluid toward the hot side. In detail, the fluctuations at the hot wall follow a convex trajectory peaking at $y^+ \approx 5$–7 with value $T^+_{\mathrm{rms}} \approx 1.5$, whereas for the cold wall the fluctuations present a maximum of $T^+_{\mathrm{rms}} \approx 6.5$ at $y^+ \approx 15$, followed by an oscillatory shape with a minimum of $T^+_{\mathrm{rms}} \approx 5.0$ at $y^+ \approx 60$. In connection to the temperature distribution, Fig. 9 depicts the variation of time-averaged ρ/ρ_c, with $\rho_c \approx 313\,\mathrm{kg/m^3}$ the critical density, along the wall-normal direction for the cold and hot walls. The results indicate that (i) the most rapid variations of density are found in the buffer layers of the two walls, and (ii) density reaches the critical value toward the

TABLE I. Friction Reynolds, Prandtl, and Nusselt numbers for the low- and high-pressure cases.

	Wall	Re_τ	Pr	Nu
Low-pressure	Both	100	0.71	–
High-pressure	Cold	100	2.14	5.75
	Hot	176.38	0.97	21.47

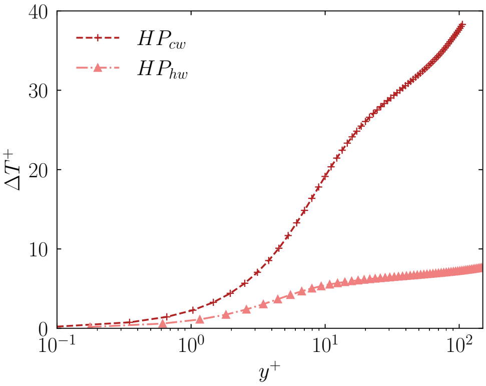

FIG. 7. Time-averaged increment of temperature ΔT^+ along the wall-normal direction y^+ for the cold (cw) and hot (hw) walls of the high-pressure (HP) case.

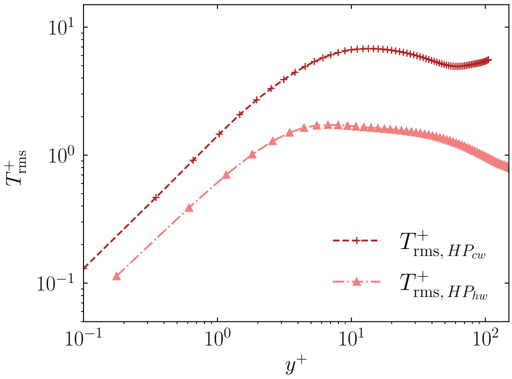

FIG. 8. Favre-averaged fluctuations of temperature T^+_{rms} along the wall-normal direction y^+ for the cold (cw) and hot (hw) walls of the high-pressure (HP) case.

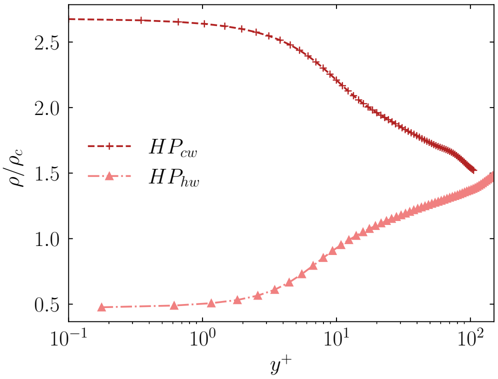

FIG. 9. Time-averaged density ρ/ρ_c along the wall-normal direction y^+ for the cold (cw) and hot (hw) walls of the high-pressure (HP) case.

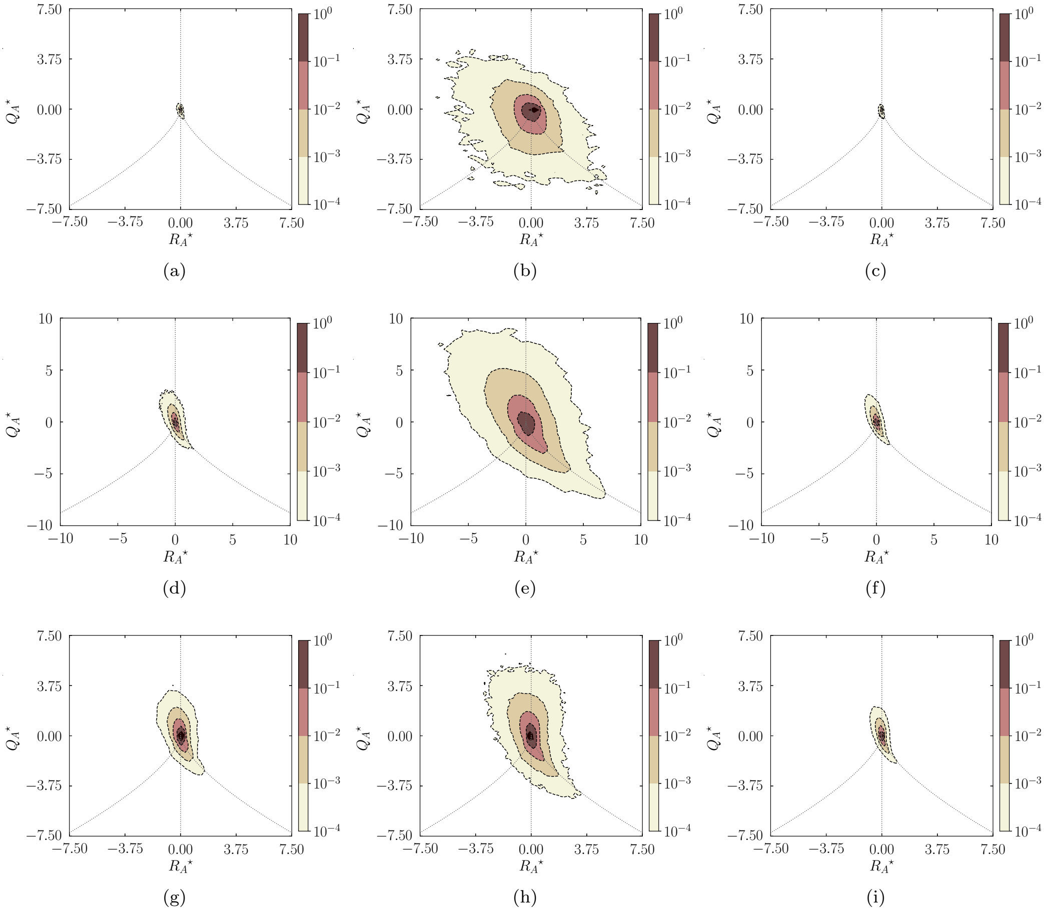

(a) (b) (c)

(d) (e) (f)

(g) (h) (i)

FIG. 10. JPDFs of the second and third velocity-gradient tensor invariants for the small scales of the flow. Columns correspond to: HP cold wall (first), HP hot wall (second), and LP (third). Rows correspond to: viscous sublayer (first), buffer layer (second), and log-law region (third).

center of the channel. In particular, the buffer layer of the hot/top wall is where the pseudoboiling region is mostly located in a time-averaged sense.

D. Velocity-gradient tensor invariants

The topology of turbulent flow motions at different scales is analyzed in this section. Similar to the work by Blackburn *et al.* [41], the analyses are based on JPDFs of the velocity-gradient tensor invariants, which are described in Sec. II, conditioned on distance from the walls. In particular, the characterization is performed at two scales corresponding to (i) the smallest flow motions and (ii) at a scale comparable to the density gradient scale estimated in Sec. IV B. Additionally, the invariants are normalized as $Q_i{}^* = Q_i(\delta/u_b{}^2)$ and $R_i{}^* = R_i(\delta/u_b{}^3)$, where subscript i refers to the different tensors A, S, and W. Focusing first on the smallest flow scales, Fig. 10 displays the JPDFs of the second and third invariants of the velocity-gradient tensor conditioned on different distances from the walls. Upon observation of the three sets of JPDFs, it can be noted the similarity between the distributions of the cold wall of the HP case (first column) and the LP setup (third column). These distributions indicate that the smallest flow scales tend to present a higher tendency for vortical events as they separate from the wall, which is typical in wall-bounded isothermal turbulent flow

[41]. Specifically, the data for these two columns (first and third) is spread across the SFS and UN/S/S regions, which is indicative of a tendency of divergent stretching motions as schematically represented in Fig. 1. However, the most notable differences with respect to the reference LP case are found in the hot wall region of the HP setup. Particularly, in the viscous sublayer, the distribution of data is noticeably more spread, indicating the presence of a wider range of intensities of the near-wall motions; this behavior is usually found in regions far from the wall. Moreover, the existence of a more rounded distribution for the most probable events indicates that the small scales of the flow do not present a clear preference for a specific topology; viz. flow motions are balanced between divergent and convergent trajectories and tube- and sheetlike structures. As it will be studied in Sec. IV E, this result is an important characteristic of the hot region of the HP case as it will contribute to a notable increase of the effects of derived flow variables, like, for example, vorticity and dissipation. Regarding the other two wall regions (second and third rows), the flow topologies present distributions more aligned with the typical behavior of isothermal turbulence in which there is a predominance of vortex stretching and dissipative events as indicated by the characteristic teardrop shape [39].

The analysis continues by focusing on the JPDFs of the second and third invariants of the rate-of-strain tensor for the smallest flow scales depicted in Fig. 11. Two main topologies need to be considered. First, disklike structures tend to be formed by convergent flow trajectories when data is distributed toward the axisymmetric expansion line (right side of the Q_S-R_S diagram). Alternatively, if the data is skewed toward the axisymmetric contraction line (left side of the Q_S-R_S diagram), then rodlike structures tend to be generated by divergent flow trajectories. In this regard, similar to Fig. 10, the distributions in Figs. 11(a), 11(c) 11(d), 11(f), 11(g), and 11(i) show analogous shapes: (i) predominance of disklike topologies connected to high dissipation rates in the viscous sublayer due to wall constraints, whereas (ii) data tends to be biased toward the axisymmetric expansion line (rodlike topologies) as it separates from the wall. Related to the distributions of the HP hot wall, the most probable topologies are found along the ${R_S}^*$ axis, corresponding to the two-dimensional straining limit, which, for the case of large negative ${Q_S}^*$ values, contributes to generating high levels of dissipation. For the viscous sublayer region (first row), it is, however, important to highlight the significant difference (roughly 3–5×) in magnitude of the HP hot wall with respect to the reference LP and HP cold wall cases. Concentrating in the buffer layer (second row), the most probable flow motions do not present any particular dominant trend as both axisymmetric contraction and expansion lines contain similar amounts of data, which is typically referred to as biaxial strain. Consequently, the high levels of dissipation observed near the HP hot wall, in addition to the large density variations across the pseudoboiling region mostly contained within the buffer layer of this wall, are probably responsible for modifying the standard topologies from axisymmetric expansion toward biaxial strain. Finally, the distributions corresponding to the log-law region (third row) are similar to the canonical LP distributions, where data is biased toward the axisymmetric expansion lines following convergent trajectories.

The examination of the small-scale topologies culminates by studying the ratio between the second invariant of the rate-of-strain and rate-of-rotation tensors depicted in Fig 12. Starting with the viscous sublayer (first row), it can be observed that neither strain nor rotation events dominate as the distributions lay along the 45 line, which is the usual behavior for isothermal wall-bounded turbulent flow. However, the maximum magnitudes for the HP hot wall are 3× larger compared to other two cases, suggesting the presence of more intense shear and rotation motions in that region. These flow motions tend to create the structures observed by Blackburn *et al.* [41], and highlighted by Soria *et al.* [39], known as vortex sheets. Throughout this region, as it will be characterized in Sec. IV E, vorticity values are the highest resulting in large mixing rates. This high level of vorticity is attenuated in the buffer layer (second row), which is connected to lower values of dissipation. In addition, the small skewness along the ${Q_W}^*$ axis suggests a slight predominance of rotationlike motions over shear-related topologies. However, despite the fact that the distribution is evenly balanced between both axes in the HP case, the more probable events in the logarithmic

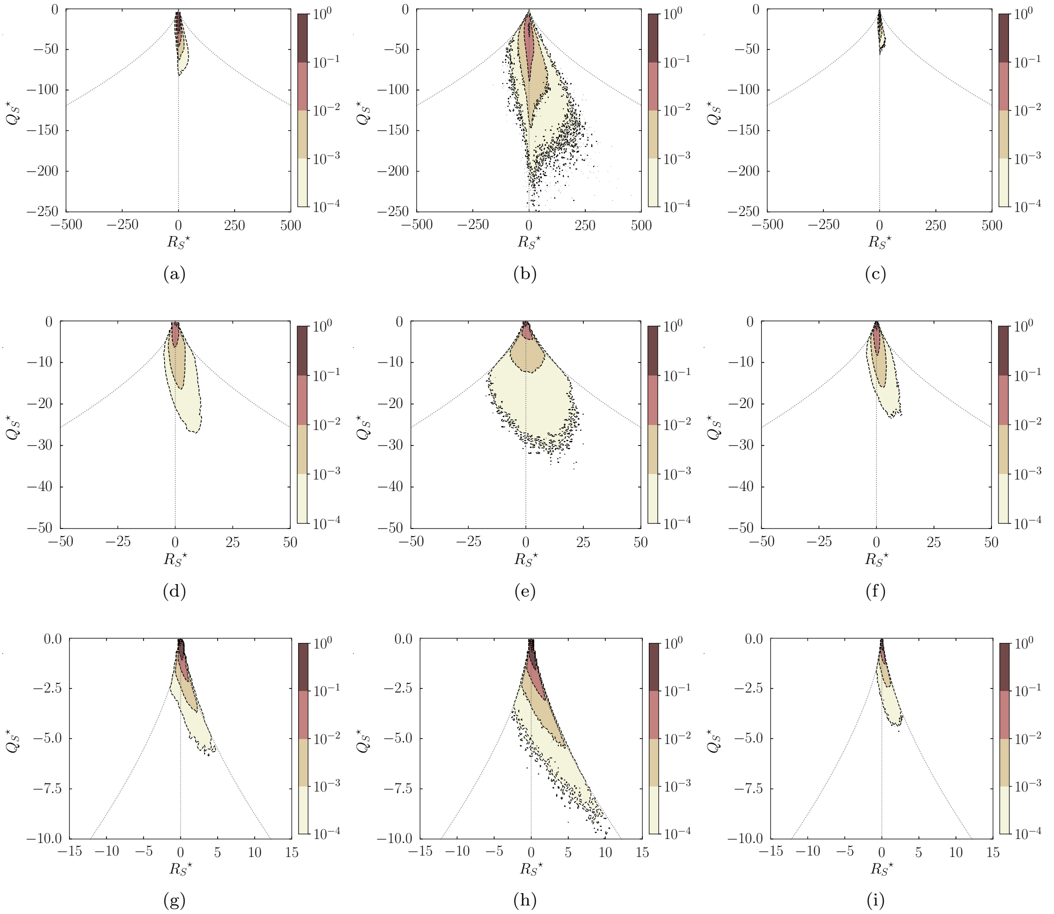

FIG. 11. JPDFs of the second and third rate-of-strain tensor invariants for the small scales of the flow. Columns correspond to: HP cold wall (first), HP hot wall (second), and LP (third). Rows correspond to: viscous sublayer (first), buffer layer (second), and log-law region (third).

layer are slightly skewed toward rotation motions. Moreover, it is important to highlight that vortex sheet structures become less dominant away from walls.

As certain differences have been observed between (especially) the HP hot wall and the reference LP case, flow topologies are further characterized by focusing at spatial lengths comparable to the density gradient scale estimated in Sec. IV B. The selection of this scale, as discussed in Sec. IV E, is based on the fact that density variations are notably responsible, through a baroclinic-type instability, for modifying the flow structures with respect to the standard isothermal LP case. In this regard, JPDFs results of flow topologies at this larger scale are depicted in Fig. 13 for the center region contained between $y_{\mathrm{bw}}^{+} \approx 30$ and $y_{\mathrm{tw}}^{+} \approx 55$. Two main observations can be inferred from the figure. First, as shown in Figs. 13(a)–13(d) and analogously to the small scales, similar distributions are observed for the HP and LP cases for the second and third invariants of the velocity-gradient and rate-of-strain tensors. Second, the distributions for the ratio between the second invariant of the rate-of-strain and rate-of-rotation tensors depicted in Figs. 13(e) and 13(f), however, present notably different shapes: roundlike for HP hot wall, and arrowedlike for LP. Regarding the arrowed distribution, data is mostly concentrated along the 45 line, which highlights the predominance of vortex sheets structures. These vortical-like motions are considered to be more dissipative and

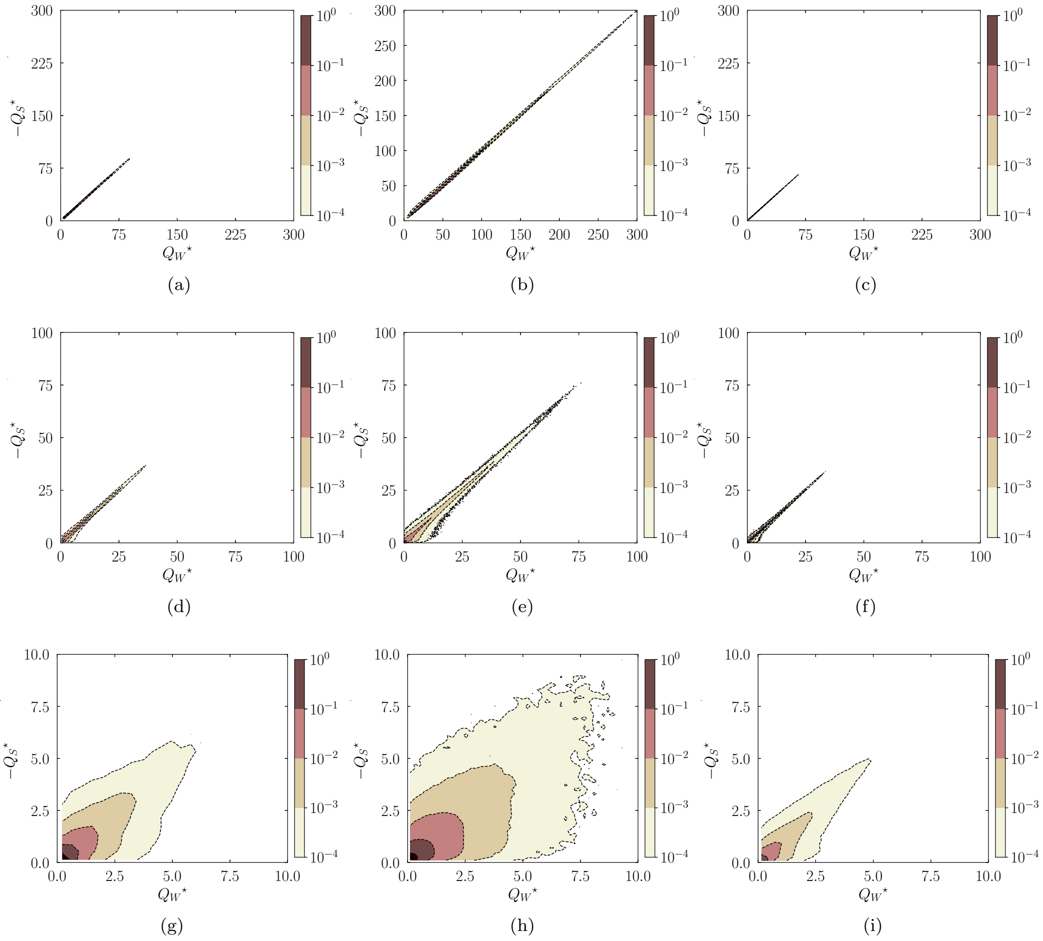

(a) (b) (c)

(d) (e) (f)

(g) (h) (i)

FIG. 12. JPDFs of the second rate-of-strain and rate-of-rotation tensor invariants for the small scales of the flow. Columns correspond to: HP cold wall (first), HP hot wall (second), and LP (third). Rows correspond to: viscous sublayer (first), buffer layer (second), and log-law region (third).

associated to larger enstrophy values, which form rollers as they develop in time. Thus, for the LP case, the turbulent flow topologies behave similarly at the small and density-gradient scales since similar distributions are observed. On the contrary, the rounder shapes close to the origin observed for the HP hot wall case suggest a larger likelihood of finding vortex tube structures associated with irrotational dissipation mechanism. These structures are typically less dissipative than vortex sheets, and are connected to the high values of vortex stretching and baroclinic torque shown in Figs. 14(b) and 14(c).

E. Vorticity transport decomposition

As previously introduced, to characterize the intrinsic flow mechanisms responsible for the higher levels of flow fluctuations identified close to the hot wall of the HP system, which can be linked to vorticity generation and distribution as discussed below, the vorticity transport equation is considered as follows:

$$\frac{\partial \boldsymbol{\omega}}{\partial t} + (\boldsymbol{u} \cdot \nabla)\boldsymbol{\omega} = (\boldsymbol{\omega} \cdot \nabla)\boldsymbol{u} - \boldsymbol{\omega}(\nabla \cdot \boldsymbol{u}) + \frac{1}{\rho^2}\nabla\rho \times \nabla P + \nabla \times \left(\frac{1}{\rho}\nabla \cdot \boldsymbol{\tau}\right), \tag{15}$$

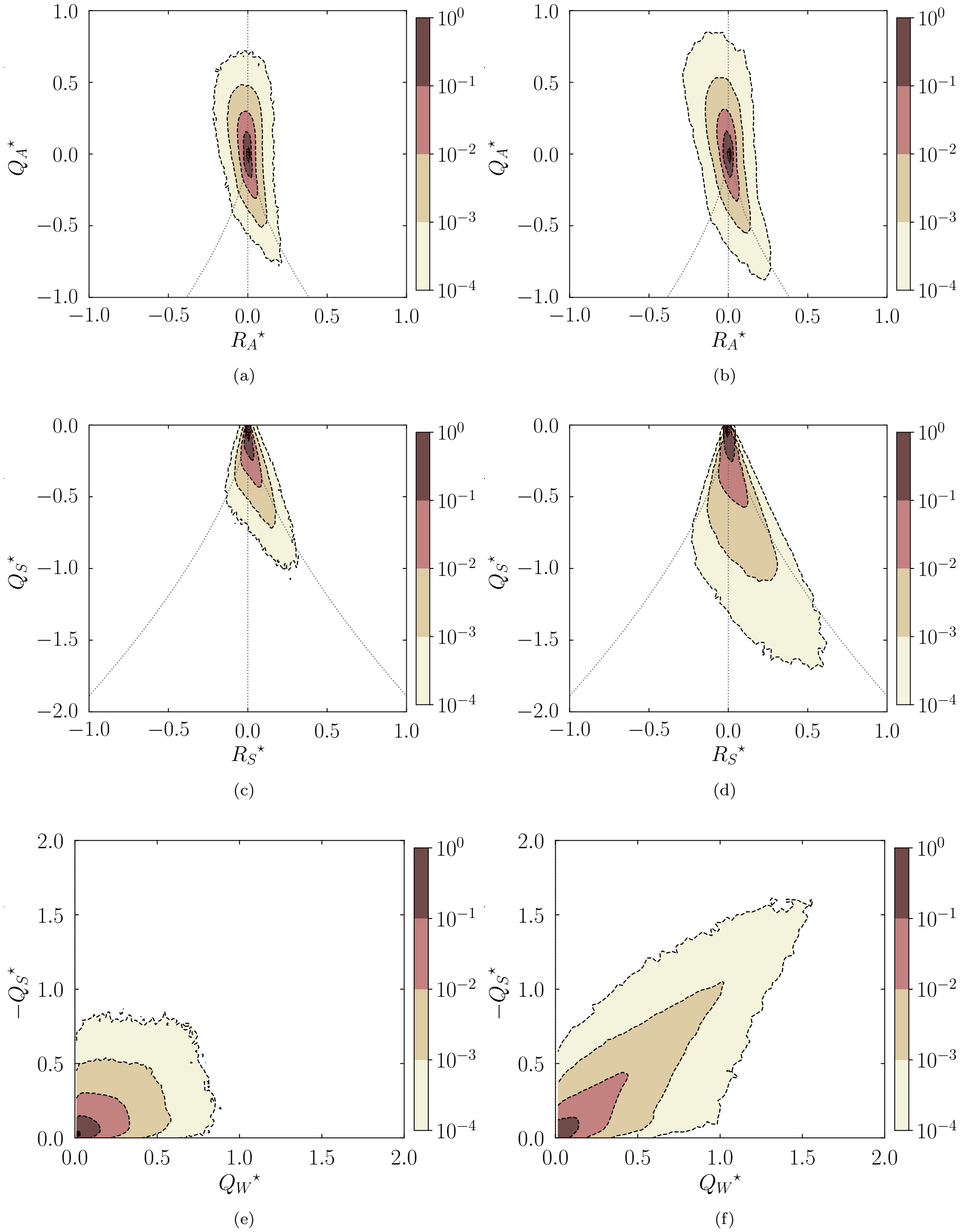

FIG. 13. JPDFs at the density gradient scale of the flow. Columns correspond to: HP (first), LP (second). Rows correspond to: Q_A versus R_A (first), Q_S versus R_S (first), and $-Q_S$ versus Q_W (third).

where $\boldsymbol{\omega} = \nabla \times \boldsymbol{u}$ is the vorticity vector, $\frac{D\boldsymbol{\omega}}{Dt} = \frac{\partial \boldsymbol{\omega}}{\partial t} + (\boldsymbol{u} \cdot \nabla)\boldsymbol{\omega}$ is the material derivative containing the temporal and advection terms, $(\boldsymbol{\omega} \cdot \nabla)\boldsymbol{u} - \boldsymbol{\omega}(\nabla \cdot \boldsymbol{u})$ is the vortex stretching mechanism, $(1/\rho^2)\nabla\rho \times \nabla P$ is the baroclinic torque with ∇P resulting from the external force driving the flow in the streamwise direction, and $\nabla \times (\frac{1}{\rho}\nabla \cdot \boldsymbol{\tau})$ is the dissipation of the viscous stresses. It is

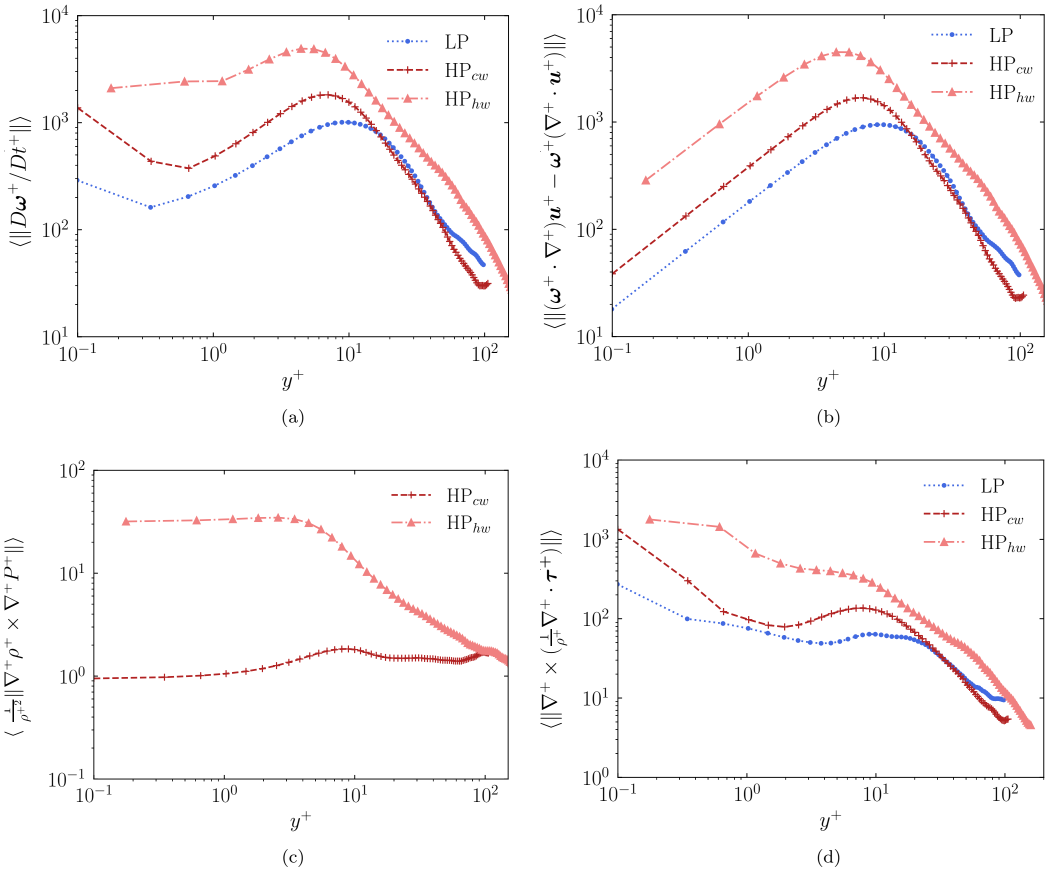

(a)

(b)

(c)

(d)

FIG. 14. Magnitude of the vorticity transport terms for the HP and LP cases: (a) material derivative, (b) vortex stretching, (c) baroclinic torque, and (d) viscous diffusion; all terms are normalized by $(u_\tau/\delta)^2$.

important to note that the baroclinic torque term becomes important at the regions of the HP case where density variations are large, i.e., across the pseudoboiling line. In those regions, the cross product between the imposed pressure difference and density gradients results in the generation of intense vortical motions that contribute to the destabilization of the flow and the subsequent increase in turbulent fluctuations.

The total and decomposed terms of the vorticity transport equation normalized by $(u_\tau/\delta)^2$ are shown in Fig. 14 for the HP and LP cases based on ensemble-averaged quantities of 10 snapshots at different FTTs. Four principal observations can be inferred from the results. First, as it can be seen in Fig. 14(a), the HP system (especially the hot wall) exhibits larger magnitudes of vorticity transport compared to the reference LP case; viz. almost an order of magnitude larger for the hot wall in the viscous sublayer and buffer layer. Second, for the HP and LP cases, the vortex stretching mechanism quantified in Fig. 14(b) presents peak values in the buffer layer. However, this mechanism is more intense for the hot wall of the HP system as it presents values that are roughly 5× larger than for the LP case. This observation can be related to Fig. 12(b) where data is concentrated along the 45 line, which is indicative of a predominance of vortex sheets structures responsible for enhanced dissipation; this result is reinforced by Fig. 11(b) in which the invariant $Q_S{}^*$ presents significantly larger negative values. Third, regarding the baroclinic torque for the HP case (which is negligible for the isothermal LP system), Fig. 14(c) shows a difference of approximately 30× between the hot and cold walls. This large difference is caused by the strongly localized density gradients found in the vicinity of the hot wall. In particular, due to angular momentum conservation, the baroclinic torque generated increases the amount of flow rotation, which in turn enhances the importance of vortex stretching mechanisms. Moreover, as observed in Fig. 13, the flow instabilities generated by this baroclinic torque contribute also to the formation of vortex tubes of a size similar to the density gradient scale. Finally (fourth observation), as a result of higher vorticity levels, the viscous stresses depicted in Fig. 14(d) indicate that vorticity dissipation is almost an order of magnitude larger for the hot wall of the HP system than for the reference LP case, which is indicative of the presence of more intense turbulent motions in the former.

V. SUMMARY AND CONCLUSIONS

This work has aimed at studying the multiscale flow topologies of microconfined high-pressure transcritical turbulent channel flow based on velocity-field tensor invariants. In this regard, first, the principal hydrodynamic scales of the problem have been estimated based on scaling arguments. Second, the main features of the turbulent flow have been characterized by means of first- and second-order flow statistics. Third, the invariants of the velocity-gradient, rate-of-strain, and rate-of-rotation tensors have been analyzed at different length scales through the distributions represented by JPDFs. Finally, the unique features of the turbulent flow have been comprehensively studied by leveraging the insight provided by the variable-density vorticity transport equation.

The computational results obtained in this work have revealed distinct flow topologies for the HP system with respect to the LP reference case, especially in the hot region where the largest density gradients are mostly found. In particular, for the hot wall of the HP case, the second and third invariants of the velocity-gradient tensor present topologies typical of the outer layer near the wall region, whereas the rate-of-strain tensor reveals the presence of higher dissipation rates, which are $3-5\times$ larger in the viscous sublayer region. Additionally, the second invariant of the rate-of-rotation and rate-of-strain tensors indicates the formation of more powerful dissipative flow motions near the wall. Finally, as a result of the strong localized density variations across the pseudoboiling region, the flow topologies at spatial lengths comparable to the density gradient scale tend to favor vortex tube structures over vortex sheets. As identified from analyzing the terms composing the vorticity transport equation, this result is a consequence of the large values of baroclinic torque in that region, which are responsible for increasing the amount of vorticity in the system.

As future research, it would be very valuable to: (i) investigate how the multiscale flow topologies are impacted when varying the operating conditions of the system in terms of pressure and temperature, (ii) further study and characterize flow statistics in the vicinity of walls where the transformation models need to be adapted for high-pressure transcritical systems, (iii) expand the study to different flow configurations (e.g., boundary and mixing layers, duct flows), and (iv) analyze the kinematics of the flow topologies by considering their time evolution. Finally, once a comprehensive understanding of the flow topologies is obtained across various conditions, the ultimate step would be to develop RANS and LES models to facilitate the computational design and optimization of microconfined turbulent flow systems operating at high-pressure transcritical regimes.

ACKNOWLEDGMENTS

This work is funded by the European Union (ERC, SCRAMBLE, Grant No. 101040379). Views and opinions expressed are however those of the authors only and do not necessarily reflect those of the European Union or the European Research Council. Neither the European Union nor the granting authority can be held responsible for them. The authors also acknowledge support from the *Beatriz Galindo* program (Distinguished Researcher, Grant No. BGP18/00026) of the Ministerio de Ciencia, Innovación y Universidades (Spain), the SRG program (Grant No. 2021-SGR-01045) of the Generalitat de Catalunya (Spain), and the computer resources at FinisTerrae III and the technical support provided by CESGA (Grant No. RES-IM-2023-1-0005).

[1] D. Sinton, Energy: The microfluidic frontier, Lab Chip **14**, 3127 (2014).

[2] M. Bernades and L. Jofre, Thermophysical analysis of microconfined turbulent flow regimes at supercritical fluid conditions in heat transfer applications, J. Heat Transfer **144**, 082501 (2022).

[3] K. R. Sreenivasan, Turbulent mixing: A perspective, Proc. Natl. Acad. Sci. USA **116**, 18175 (2019).

[4] S. Hardt and F. Schönfeld, *Microfluidic Technologies for Miniaturized Analysis Systems*, 1st ed. (Springer, Cambridge, MA, 2007).

[5] M. Hoffmann, M. Schlüter, and N. Räbiger, Experimental investigation of liquid-liquid mixing in T-shaped micro-mixers using μ-LIF and μ-PIV, Chem. Eng. Sci. **61**, 2968 (2006).

[6] R. Lindken, J. Westerweel, and B. Wieneke, Stereoscopic micro particle image velocimetry, Exp. Fluids **41**, 161 (2006).

[7] K. Nan, Z. Hu, W. Zhao, K. Wang, J. Bai, and G. Wang, Large-scale flow in micro electrokinetic turbulent mixer, Micromachines **11**, 813 (2020).

[8] J. B. You, K. Kang, T. T. Tran, H. Park, W. R. Hwang, J. M. Kim, and S. G. Im, PDMS-based turbulent microfluidic mixer, Lab Chip **15**, 1727 (2015).

[9] M. Rossi, R. Lindken, B. P. Hierck, and J. Westerweel, Tapered microfluidic chip for the study of biochemical and mechanical response at subcellular level of endothelial cells to shear flow, Lab Chip **9**, 1403 (2009).

[10] S. W. Stone, C. D. Meinhart, and S. T. Wereley, A microfluidic-based nanoscope, Exp. Fluids **33**, 613 (2002).

[11] C. M. Zettner and M. Yoda, Particle velocity field measurements in a near-wall flow using evanescent wave illumination, Exp. Fluids **34**, 115 (2003).

[12] B. J. Kim, Y. Z. Liu, and H. J. Sung, Micro piv measurement of two-fluid flow with different refractive indices, Meas. Sci. Technol. **15**, 1097 (2004).

[13] A. Günther, S. A. Khan, M. Thalmann, F. Trachsel, and K. F. Jensen, Transport and reaction in microscale segmented gas-liquid flow, Lab Chip **4**, 278 (2004).

[14] H. Kinoshita, S. Kaneda, T. Fujii, and M. Oshima, Three-dimensional measurement and visualization of internal flow of a moving droplet using confocal micro-PIV, Lab Chip **7**, 338 (2007).

[15] Y. Liu, M. G. Olsen, and R. O. Fox, Turbulence in a microscale planar confined impinging-jets reactor, Lab Chip **9**, 1110 (2009).

[16] P. Hao, F. He, and K. Zhu, Flow characteristics in a trapezoidal silicon microchannel, J. Micromech. Microeng. **15**, 1362 (2005).

[17] M. Bernades, F. Capuano, and L. Jofre, Flow physics characterization of microconfined high-pressure transcritical turbulence, in *Proceedings of the Summer Program 2022*, Center for Turbulence Research (Stanford University, 2022), p. 215.

[18] M. Bernades, F. Capuano, and L. Jofre, Microconfined high-pressure transcritical fluids turbulence, Phys. Fluids **35**, 015163 (2023).

[19] J. Y. Yoo, The turbulent flows of supercritical fluids with heat transfer, Annu. Rev. Fluid Mech. **45**, 495 (2013).

[20] L. Jofre and J. Urzay, Transcritical diffuse-interface hydrodynamics of propellants in high-pressure combustors of chemical propulsion systems, Prog. Energy Combust. Sci. **82**, 100877 (2021).

[21] L. Jofre and J. Urzay, A characteristic length scale for density gradients in supercritical monocomponent flows near pseudoboiling, in *Annual Research Briefs*, Center for Turbulence Research (Stanford University, 2020), p. 277.

[22] X. Cheng and X. J. Liu, Research challenges of heat transfer to supercritical fluids, J. Nuclear Rad. Sci. **4**, 011003 (2018).

[23] F. Zhang, S. Marre, and A. Erriguible, Mixing intensification under turbulent conditions in a high pressure microreactor, Chem. Eng. J. **382**, 122859 (2020).

[24] V. V. Lemanov, V. I. Terekhov, K. A. Sharov, and A. A. Shumeiko, An experimental study of submerged jets at low Reynolds numbers, Tech. Phys. Lett. **39**, 421 (2013).

[25] A. Patel, B. J. Boersma, and R. Pecnik, The influence of near-wall density and viscosity gradients on turbulence in channel flows, J. Fluid Mech. **809**, 793 (2016).

[26] P. C. Ma, X. I. A. Yang, and M. Ihme, Structure of wall-bounded flows at transcritical conditions, Phys. Rev. Fluids **3**, 034609 (2018).

[27] K. Kim, J. P. Hickey, and C. Scalo, Pseudophase change effects in turbulent channel flow under transcritical temperature conditions, J. Fluid Mech. **871**, 52 (2019).

[28] T. Toki, S. Teramoto, and K. Okamoto, Velocity and temperature profiles in turbulent channel flow at supercritical pressure, J. Propul. Power **36**, 3 (2020).

[29] A. Trettel and J. Larsson, Mean velocity scaling for compressible wall turbulence with heat transfer, Phys. Fluids **28**, 026102 (2016).

[30] K. P. Griffin, L. Fu, and P. Moin, Velocity transformation for compressible wall-bounded turbulent flows with and without heat transfer, Proc. Natl. Acad. Sci. USA **118**, e2111144118 (2021).

[31] K. Younes and J.-P. Hickey, Mean velocity scaling of high-speed turbulent flows under nonadiabatic wall conditions, AIAA J. **61**, 1532 (2023).

[32] A. Patel, B. J. Boersma, and R. Pecnik, Scalar statistics in variable property turbulent channel flows, Phys. Rev. Fluids **2**, 084604 (2017).

[33] J. Guo, X. I. A. Yang, and M. Ihme, Structure of the thermal boundary layer in turbulent channel flows at transcritical conditions, J. Fluid Mech. **934**, A45 (2022).

[34] D. C. Wilcox, *Turbulence Modeling for CFD* (DCW Industries, Incorporated, La Cañada, CA, 1998).

[35] L. Jofre, S. P. Domino, and G. Iaccarino, A framework for characterizing structural uncertainty in large-eddy simulation closures, Flow, Turbul. Combust. **100**, 341 (2018).

[36] L. Jofre, S. P. Domino, and G. Iaccarino, Eigensensitivity analysis of subgrid-scale stresses in large-eddy simulation of a turbulent axisymmetric jet, Int. J. Heat Fluid Flow **77**, 314 (2019).

[37] A. E. Perry and M. S. Chong, A description of eddying motions and flow patterns using critical-point concepts, Annu. Rev. Fluid Mech. **19**, 125 (1987).

[38] M. S. Chong and A. E. Perry, A general classification of three-dimensional flow fields, Phys. Fluids **2**, 765 (1990).

[39] J. Soria, R. Sondergaard, B. J. Cantwell, M. S. Chong, and A. E. Perry, A study of the fine-scale motions of incompressible time-developing mixing layers, Phys. Fluids **6**, 871 (1994).

[40] O. N. Boratav and R. B. Pelz, On the local topology evolution of a highsymmetry flow, Phys. Fluids **7**, 1712 (1995).

[41] H. M. Blackburn, N. N. Mansour, and B. J. Cantwell, Topology of fine-scale motions in turbulent channel flow, J. Fluid Mech. **310**, 269 (1996).

[42] C. B. da Silva and J. C. F. Pereira, Invariants of the velocity-gradient, rate-of-strain, and rate-of-rotation tensors across the turbulent/nonturbulent interface in jets, Phys. Fluids **20**, 055101 (2008).

[43] M. S. Dodd and L. Jofre, Small-scale flow topologies in decaying isotropic turbulence laden with finite-size droplets, Phys. Rev. Fluids **4**, 064303 (2019).

[44] S. Suman and S. S. Girimaji, Velocity gradient invariants and local flow-field topology in compressible turbulence, JoT **11**, 1 (2010).

[45] C. Meneveau, Lagrangian dynamics and models of the velocity gradient tensor in turbulent flows, Annu. Rev. Fluid Mech. **43**, 219 (2011).

[46] D. Y. Peng and D. B. Robinson, A new two-constant equation of state, Ind. Eng. Chem. Fund. **15**, 59 (1976).

[47] W. C. Reynolds and P. Colonna, *Thermodynamics: Fundamentals and Engineering Applications*, 1st ed. (Cambridge University Press, Cambridge, UK, 2019).

[48] A. Burcat and B. Ruscic, Third millennium ideal gas and condensed phase thermochemical database for combustion (with updates from active thermochemical tables), Tech. Rep. No. ANL-05/20 (Argonne National Laboratory, Argonne, IL, USA, 2005).

[49] T. H. Chung, L. L. Lee, and K. E. Starling, Applications of kinetic gas theories and multiparameter correlation for prediction of dilute gas viscosity and thermal conductivity, Ind. Eng. Chem. Fund. **23**, 8 (1984).

[50] T. H. Chung, M. Ajlan, L. L. Lee, and K. E. Starling, Generalized multiparameter correlation for nonpolar and polar fluid transport properties, Ind. Eng. Chem. Res. **27**, 671 (1988).

[51] B. E. Poling, J. M. Prausnitz, and J. P. OConnell, *Properties of Gases and Liquids*, 5th ed. (McGraw Hill, New York, 2001).

[52] S. Gottlieb, C.-W. Shu, and E. Tadmor, Strong stability-preserving high-order time discretization methods, SIAM Rev. **43**, 89 (2001).

[53] G. Coppola, F. Capuano, S. Pirozzoli, and L. de Luca, Numerically stable formulations of convective terms for turbulent compressible flows, J. Comput. Phys. **382**, 86 (2019).

[54] G. Coppola, F. Capuano, and L. de Luca, Discrete energy-conservation properties in the numerical simulation of the Navier-Stokes equations, Appl. Mech. Rev. **71**, 010803 (2019).

[55] M. Bernades, L. Jofre, and F. Capuano, Investigation of a novel numerical scheme for high-pressure supercritical fluids turbulence, in *Proceedings of the Summer Program 2022*, Center for Turbulence Research (Stanford University, 2022), p. 225.

[56] L. Jofre, A. Abdellatif, and G. Oyarzun, RHEA—An open-source reproducible hybrid-architecture flow solver engineered for academia, J. Open Source Softw. **8**, 4637 (2023).

[57] K. S. Nelson and O. B. Fringer, Reducing spin-up time for simulations of turbulent channel flow, Phys. Fluids **29**, 105101 (2017).

[58] Q. Wang, X. Ma, J. Xu, M. Li, and Y. Wang, The three-regime-model for pseudoboiling in supercritical pressure, Int. J. Heat Mass Transf. **181**, 121875 (2021).

[59] R. D. Moser, J. Kim, and N. N. Mansour, Direct numerical simulation of turbulent channel flow up to re 590, Phys. Fluids **11**, 943 (1999).